Silicon (2024) 16:1343–1356
https://doi.org/10.1007/s12633-023-02762-3

RESEARCH

Investigation of the Influence of Solid–Liquid Interface Shape Based on the Jordan Model on Cz-Silicon Dislocation Defects

Tai Li[1] · Liang Zhao[2] · Zhenling Huang[1] · Liang Zhao[1] · Yindong Shi[1] · Shaoyun Li[1] · Yongsheng Ren[1] · Guoqiang Lv[1] · Wenhui Ma[1]

Received: 25 September 2023 / Accepted: 8 November 2023 / Published online: 18 November 2023
© The Author(s), under exclusive licence to Springer Nature B.V. 2023

Abstract
During the growth of Czochralski single crystal silicon, the change of solid–liquid interface shape leads to uneven distribution of thermal stress, and the concentration of thermal stress leads to crystal defects in the process of single crystal formation, which reduces the efficiency of solar cells. In order to avoid a large number of crystal defects caused by the concentration of thermal stress near the solid–liquid interface, the effect of the solid–liquid interface shape on thermal stresses is investigated in this study using numerical calculations to determine the most favourable solid–liquid interface shape for single crystal silicon growth. The results show that the von Mises stress on the m-shaped solid–liquid interface is smaller; von Mises stress distribution on the solid–liquid interface of a shape is more uniform; the von Mises stress on the solid–liquid interface of the n-shaped solid–liquid interface is large, and the von Mises stress can be released by controlling the solid–liquid flipping through a small range of pulling speed fluctuations, thereby reducing defects in single-crystal silicon.

Keywords Czochralski method · Single-crystal silicon · Solid–liquid interface · Von-Mises stress field · Dislocation

1 Introduction

The escalating global energy crisis can be addressed in part by harnessing solar energy, as evidenced by the International Energy Agency's 2020 World Energy Outlook report (IEA, 2020) [1]. Single-crystal silicon is extensively utilized in the photovoltaic sector for the production of solar panels [2], with Czochralski growth being the main approach for the growth of the photovoltaic single-crystal silicon [3]. Czochralski single-crystal silicon (Cz-Si) solar cells currently account for approximately 75% of the total output of photovoltaic modules, with the photovoltaic market share expected to reach 90% in 2023 [4].

Although the implementation of Dash-neck has removed the most severe effects of dislocations [5], photovoltaic Cz-Si is usually not entirely defect-free [6]. Grown-in defects in Si crystals are formed by the aggregation of excess vacancies (V) or self-interstitials (I) introduced from the solid–liquid (S-L) interface [7]. According to Voronkov theory, the value of V/G ratio determines the defect type in single crystal silicon, V- or I-dominant, V/G is defined as the growth rate (V) over the temperature gradient in the growth direction near the S-L interface (G) [8, 9]. The critical value of V/G ($(V/G)_{cri} = \xi_{cri}$) depends on both the shape of the S-L interface [10, 11] and thermal stresses at the interface [12, 13]. V-dominance occurs when the actual V/G value exceeds the V/G critical value ($(V/G)_{act} > \xi_{cri}$). A crystal will be V-dominant if the actual V/G value is greater than the critical value ($(V/G)_{act} > \xi_{cri}$), whereas if the actual V/G value is less than the critical value ($(V/G)_{act} < \xi_{cri}$), it will be I-dominant [7]. If the actual V/G ratio approaches the critical value of V/G ratio ($(V/G)_{act} \to \xi_{cri}$), it can effectively reduce the occurrence of defects during silicon single crystal growth. Nevertheless, it is very difficult to detect the S-L interface in the actual production process of Czochralski

✉ Guoqiang Lv
lvguoqiang_ok@aliyun.com

✉ Wenhui Ma
mwhsilicon@126.com

[1] Engineering Research Center for Silicon Metallurgy and Silicon Materials of Yunnan Provincial Universities, Faculty of Metallurgical and Energy Engineering, Kunming University of Science and Technology, Kunming 650093, China

[2] Qujing Yangguang Energy, Si1icon Materia1 Co.,Ltd., Qujing 655000, China

silicon single crystal. Therefore, if it is possible to predict the shape of the S-L interface and the thermal stress on the interface through calculation, this will be an important basis for the process optimization and thermal zone optimization design [14–22] of low-defect single crystal silicon.

To accurately predict the shape of the S-L interface, it is necessary to perform 3D coupling calculations [23] for the heat transfer, melt convection, and argon flow in the single crystal silicon growth furnace [11, 24]. Phil-Ouk Nam et al. used a three-dimensional numerical model to analyze the flow model inside a large single-crystal silicon furnace [25, 26]. Omidreza Asadi Noghabi and others independently carried out finite element numerical analysis and experimental research on the S-L interface during single-crystal silicon growth and found that temperature gradient, crystal phase, rotation, and crucible rotation influence the formation of W-shaped S-L interfaces [27–29]. Ran Teng et al. employed finite element numerical calculation methods in a two-dimensional model to analyze and conclude that reducing the crystallization rate leads to a flattening of the S-L interface [30]. Lijun Liu et al. employed a three-dimensional numerical model to predict the shape of the S-L interface [31]. The S-L interface has been studied through finite element numerical calculations (2D or 3D models) or experiments by many scholars, but these studies lack consideration of the continuous change of pulling speed, the relationship between S-L interface shape and thermal stress.

The purpose of this work is to find out the corresponding relationship between the shape of the S-L interface and the thermal stress when the pulling speed changes continuously during the growth of Cz-Si by numerical calculation, and to find a process and an effective method to avoid the concentration of thermal stress during the growth of single crystal silicon.

2 Model Constructions

2.1 Computational Control Equation

The melt flow and the heat transfer are governed by:

– The energy equation:

$$\rho c\left(\frac{\partial T}{\partial t}+(v\cdot\nabla)T\right)=\nabla\cdot\left(\left(k+k_T\right)\nabla T\right)+W \tag{1}$$

where T is the temperature field, ρ, c, k and k_T stand for the specific mass, specific heat, thermal conductivity and additional thermal conductivity of the medium, and W is the heat supply per unit volume.

– The continuity equation:

$$\nabla\cdot v=0 \tag{2}$$

– The momentum equation

$$\begin{aligned}\rho_0(v\cdot\nabla)v=-\nabla p+\nabla\cdot\left(\left(\mu+\mu_T\right)\left(\nabla v+\nabla^T v\right)\right)\\ -\rho_0\beta_T\left(T-T_0\right)g+J\times B\end{aligned} \tag{3}$$

where v and B are respectively the velocity field and the magnetic field, $p, \mu, \mu_T, \beta_T, g$ and J stand for the pressure, the dynamic viscosity, the additional dynamic viscosity, the volumetric expansion coefficient, the gravity and the current density. In particular, for this study $J\times B=0$.

The boundary conditions:

– Along the S-L interface:

$$T=T_m \tag{4}$$

$$-k_l\nabla T_l\cdot n=-k_s\nabla T_s\cdot n-\rho_s v_g\Delta H \tag{5}$$

– Along the melt/crystal solidification front and the melt/crucible walls, the melt should stick to the corresponding solid boundary and noslip boundary conditions are thus applied.
– Along the melt-gas interface (the socalled meniscus):

$$U\cdot\vec{n}=0 \tag{6}$$

$$\sigma_n=\chi\sigma-P_a \tag{7}$$

$$\sigma_t=\gamma_T\frac{\partial T}{\partial s} \tag{8}$$

$$f_w=\left(\tau\cdot\vec{n}\right)\cdot\vec{s} \tag{9}$$

$$\tau=\mu\left(\nabla U+\nabla U^T\right) \tag{10}$$

where T_m is the crystal melting temperature (Usually take 1685 K), n is the unit outgoing normal from the melt, v_g is the growth speed, ΔH is the latent heat of fusion per unit mass, $\vec{n}$ is the normal vector to the boundary, σ is the meniscus surface tension, σ_n is the capillary normal stress, σ_t is the meridional thermocapillary force, χ is the meniscus surface curvature, P_a is the gas pressure, γ_T is the surface tension coefficient, s is the curvilinear abscissa along the meniscus, f_w is the viscous shear stress due to the gas velocity gradients, $\vec{s}$ is the tangent vector of the meniscus, τ is the symmetric viscous stress tensor, and μ is the gas dynamic viscous. Equation (7) is used to determine the shape of the meniscus. Notice that the melt convection below the meniscus has a negligible effect on its shape due to the low capillary and Weber numbers characteristic of silicon melt flow. Therefore

the meniscus shape calculation can be decoupled from the equations governing melt convection.

For the choice of flow model, we use the mixing-length (M-L) turbulent model in FEMAG software. The additional viscosity and conductivity are given by:

$$\mu_T = \rho_0 l_m^2 \sqrt{2\underline{\boldsymbol{d}} : \underline{\boldsymbol{d}}} \tag{11}$$

$$k_T = \rho_0 c Pr_A^{-1} l_m^2 \sqrt{2\underline{\boldsymbol{d}} : \underline{\boldsymbol{d}}} \tag{12}$$

$$\underline{d} = \frac{1}{2}\left(v + {}^T v\right) \tag{13}$$

$$l_m = Cd \tag{14}$$

$$\Delta\Delta d = 0 \tag{15}$$

where $\boldsymbol{d}$ is the average rate of strain tensor, l_m is the mixing length, $\overline{Pr_A}$ is the additional Prandtl number, d is the distance to the flow boundary, C is an empirical constant, Δ is the Laplace operator. For the wall-bounded flow observed in crystal growth, it can be found experimentally that C equals the von Karman constant, or C=$k = 0.41$.

The above flow model equations have the following two shortcomings:

(1) The mixinglength estimation gets poorer in the core of the melt.
(2) It does not take the boundary layer thickness into account.

Therefore different variants of the mixing length model is proposed [32, 33]. Enhanced equations governing the distance to the boundary are proposed as follows:

$$\Delta\Delta d + \nabla \cdot (\alpha \nabla d) = 0 \tag{16}$$

$$\Delta\alpha = 0 \tag{17}$$

The boundary conditions for these two equations are detailed below for d and α:

- Along the melt/crucible and melt/crystal interfaces, the boundary conditions for d and α are [34]:

$$d = 0 \tag{18}$$

$$\alpha = \left(\frac{C}{P_c}\right)^2 \tag{19}$$

Where C and P_c may be selected as constants.

- Along the melt/axis the boundary conditions for d and α are:

$$\frac{\partial d}{\partial n} = 0 \tag{20}$$

$$\frac{\partial \alpha}{\partial n} = 0 \tag{21}$$

- Along the melt-free surface:

$$\frac{\partial \alpha}{\partial n} = 0 \tag{22}$$

For mirror condition:

$$\frac{\partial d}{\partial n} = \beta \tag{23}$$

$$\frac{\partial \Delta d}{\partial n} = 0 \tag{24}$$

For wall condition:

$$\frac{\partial d}{\partial n} = 1 \tag{25}$$

$$\frac{\partial \Delta d}{\partial n} = 0 \tag{26}$$

where n is the normal to the corresponding boundary and $\beta = 0$.

It should be noted that the mixing length boundary layer thickness can be described by combining these two constants as follows:

$$\delta = \frac{P_c}{C} \tag{27}$$

$$\delta = 5.5\left(\frac{\mu}{2\pi\rho f_D}\right)^{\frac{1}{2}} \tag{28}$$

Where μ is the dynamic viscosity, ρ is the specific mass and f_D is the rotation frequency in Hertz.

2.2 Model Description and Mesh Generation

Based on the furnace type currently being used by single-crystal silicon production enterprises, we developed a numerical calculation model based on a ratio of 1:1. As part of the numerical simulation software, we used the special numerical simulation software FEMAG for single-crystal silicon growth, which includes heat transfer, gas flow, and melt convection modules as well as von Mises stress, excess stress fields, and solidification interface shape into

the calculation. Figure 1 shows the global calculation grid and structure of the Czochralski method single-crystal silicon growth furnace. A three-dimensional model was created using the F3 module of the FEMAG software. Figure 2 shows the grid division, crystal temperature distribution, and melt flow field distribution.

The physical properties of solid silicon, liquid silicon and argon are shown in Table 1. The experimental part of our study was carried out in a production factory. To ensure the numerical model is as consistent as possible with the experiment, we have set the material properties of each structure entirely in accordance with the industrial production properties as shown in Table 2 [11, 24, 35, 36].

3 Results and Discussion

3.1 Effect of Pulling Speed on the Shape of Solid–Liquid Interface

The accuracy of the numerical model has been validated in previous research [37]. Based on the actual production process conditions, we set the crystal rotation at 8 rpm and crucible rotation at -8 rpm for the numerical model calculations.

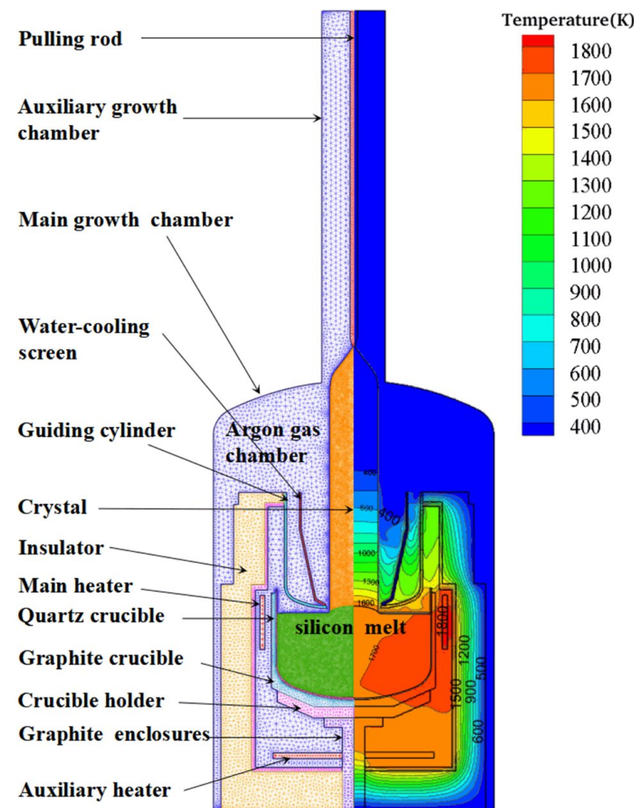

Fig. 1 Single crystal silicon furnace model calculation grid (left) and structure layout (right)

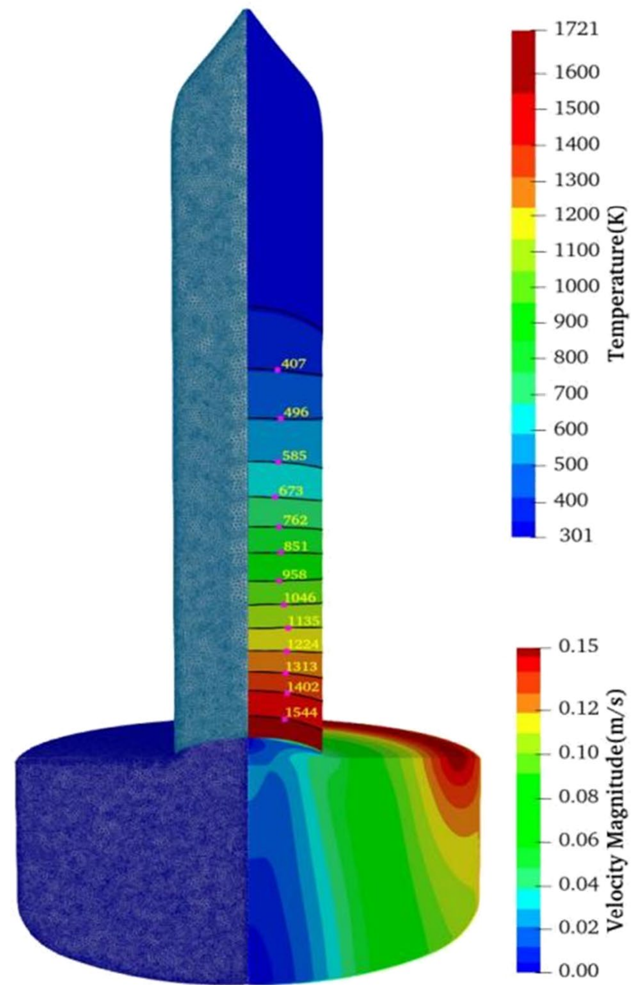

Fig. 2 The 3D modeling of silicon rods and silicon melt regions

The calculation variable is pulling speed, with a range from 0.4 mm/min to 2.2 mm/min and an increment of 0.2 mm/min. During the growth of Cz-Si, the diameter circle of the rod on the S-L interface has the lowest static thermal field temperature due to the cooling effects of the water cooling screen, and at the same time, this circle represents the junction between argon, solid silicon, and liquid silicon. Therefore, the points on this circle are also referred to as triple points. In numerical calculations, the temperature of the triple point should always be the melting point of silicon (1685 K) regardless of the dynamic thermal field prevailing during the growth of single-crystal silicon. As shown in Figs. 3 and 4, the shape of the S-L interface at different crystal pulling speeds is depicted in both 2D and 3D diagrams.

2D S-L interfaces are m-shaped when the crystal pulling speed is between 0.2 mm/min and 1.2 mm/min in the isodiametric growth stage, and as the crystal pulling speed increases, m gradually becomes flat. When the crystal pulling speed is between 1.4 mm/min and 2.2 mm/min, the

Table 1 Physical properties of silicon and argon

Material	Model construct	Variable	Value	Units
Liquid silicon	Silicon melt	Density	2420	kg/m^3
		Specific heat	1000	J/(kg·K)
		Heat conductivity	64	W/(m·K)
		Emissivity	0.33	1
		Latent heat	1805	kJ/kg
		Thermal expansion coefficient	1.41×10^{-4}	1/K
		Dynamic viscosity	7×10^{-4}	kg/(m·s)
		Diffusion coefficient for oxygen in silicon melt	5×10^{-8}	m^2/s
		Surface tension	0.874	N/m
		Surface tension coefficient	-2.8×10^{-4}	N/(m·K)
Silicon crystal	Crystal	Melting temperature	1685	K
		Density	2284.86	kg/m^3
		Specific heat	1084.66	J/(kg·K)
		Heat conductivity	$98.89–0.0943\times T+2.89\times10^{-5}\times T^2$	W/(m·K)
		Emissivity	0.7	1
		Thermal expansion coefficient	5.2×10^{-6}	1/K
		Young's modulus	1.56×10^{11}	Pa
		Poisson's ratio	0.25	1
Argon	Argon gas chamber	Specific heat	521	J/(kg·K)
		Heat conductivity	$0.0018+5.8854\times10^{-5}\times T-2.2487\times10^{-8}\times T^2+4.9213\times10^{-12}\times T^3$	W/(m·K)
		Dynamic viscosity	6.97×10^{-5}	kg/(m·s)
		Gas constant	8314	J/(K·mol)

Table 2 The physical properties of each component of single crystal silicon furnace

Component name (Material) Physical parameter (Units)		Heat conductivity W/m*K	Specific heat J/kg*K	Density kg/m^3	Emissivity 1
Main heater	pure graphite	100	2100	1750	0.7
Auxiliary heater					
Crucible holder	graphite	140	710	1700	0.7
Graphite enclosures					
Guiding cylinder	Carbon–carbon composite material	8	1800	1400	0.75
Heat insulation cylinder	Carbon–carbon composite material	10	1800	1750	0.75
Graphite crucible	Carbon–carbon composite material	40	1800	1400	0.75
Quartz crucible	quartz	1.4	2200	2530	0.5
Water-cooling screen	316L stainless steel	16.2	500	7990	0.45
Insulator	Carbon fiber	0.18	450	180	0.8
Furnace shell	304 stainless steel	16.3	500	7930	0.14
Pulling rod	Tungsten	174	130	19,250	0.3

S-L interface is n-shaped, and as the crystal pulling speed increases, n becomes more rounded. To ascertain the alteration from an m-shaped to n-shaped S-L interface, we conducted simulations to refine the pulling speed within the range of 1.2 mm/min—1.4 mm/min. The results of the calculation are presented in Fig. 5. Group one calculated the shape of the solid–liquid interface at pulling speeds between 1.22 mm/min-1.38 mm/min (Fig. 5 (a)) and group two calculated the shape at pulling speeds between 1.382 mm/min-1.398 mm/min (Fig. 5(b)). When the pulling speed gradually

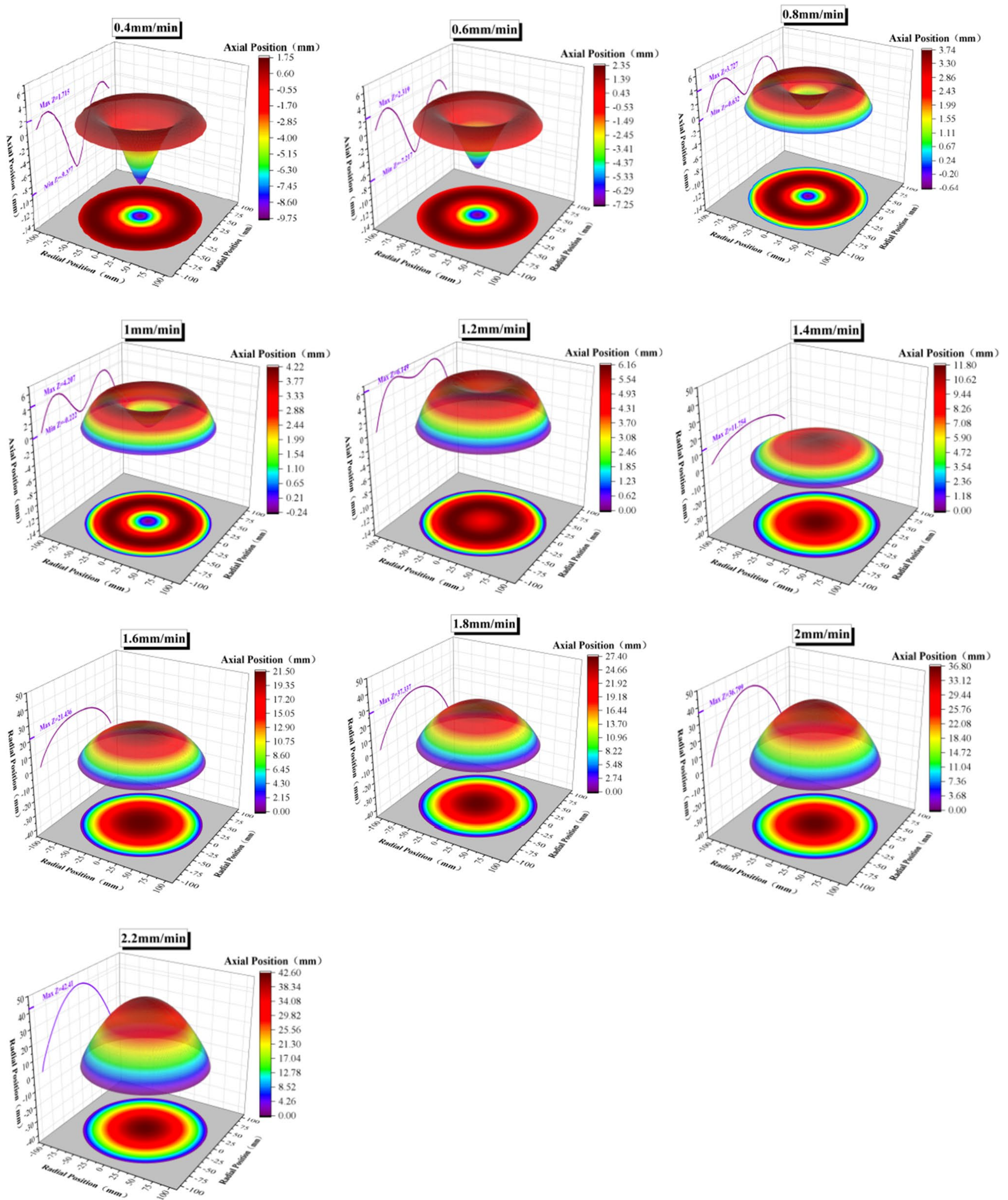

Fig. 3 3D shape of S-L interface at different pulling speeds

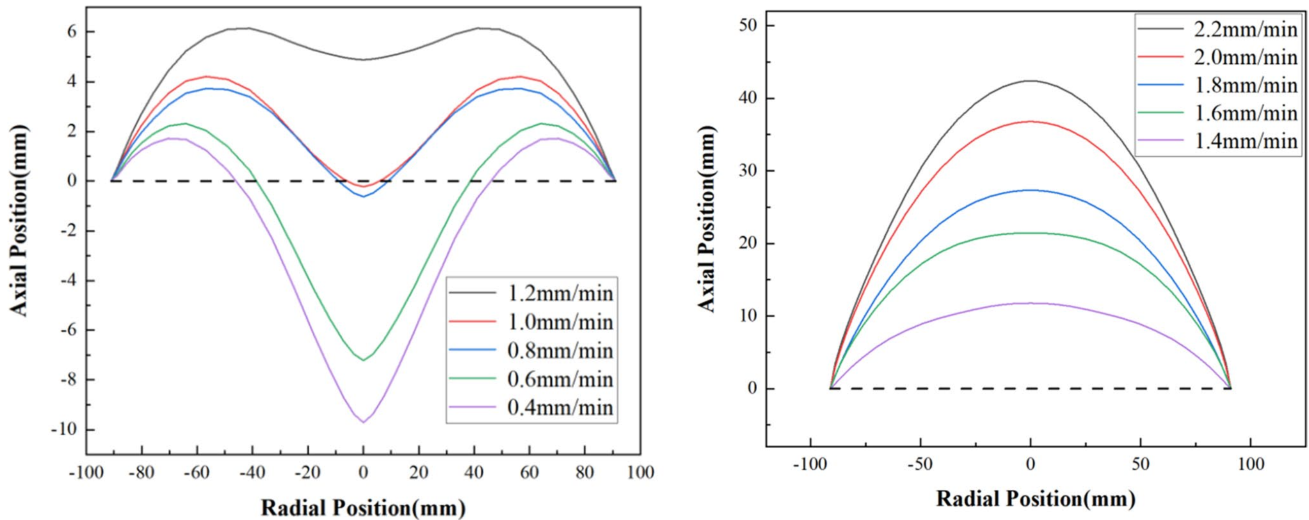

Fig. 4 2D shape of S-L interface under different pulling speeds

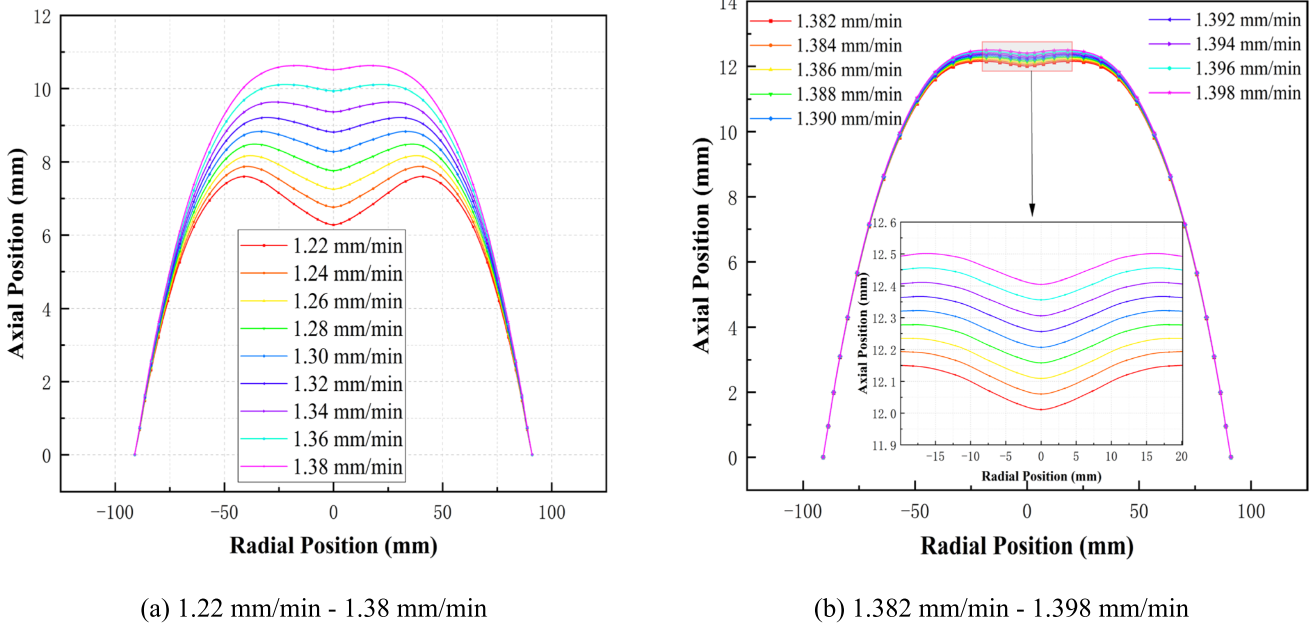

(a) 1.22 mm/min - 1.38 mm/min

(b) 1.382 mm/min - 1.398 mm/min

Fig. 5 2D shape of S-L interface under different pulling speeds (Some intermediate values of 1.2 mm / min-1.4 mm / min)

increases, the interface of a small area in the center of the S-L interface gradually becomes flat and close to —-shaped, and the whole interface is almost ⌒-shaped. During our velocity refinement calculation, we did not observe the emergence of the n-shaped S-L interface. However, based on the central local area's enlargement in Fig. 5(b), we can deduce that the m-shaped transition to the n-shaped S-L interface is probably a mutation, leading to the interface flipping, rather than a gradual and continuous process. Hence, the influence of the crystal pulling speed on the shape of S-L interfaces can be summed up as follows: the S-L interface changes from m-shape to ⌒-shape and then to n-shape as the crystal pulling speed increases.

Figure 6 shows the cross-sectional temperature distribution of the triple point. When the S-L interface is m-shaped and the crystal pulling speed is less than 0.8 mm/min, the maximum supercooling point appears at the bottom of the single-crystal silicon rod. Across a wide range of temperatures, the shape of the S-L interface is well correlated with the temperature. Suppose that the center of the single-crystal

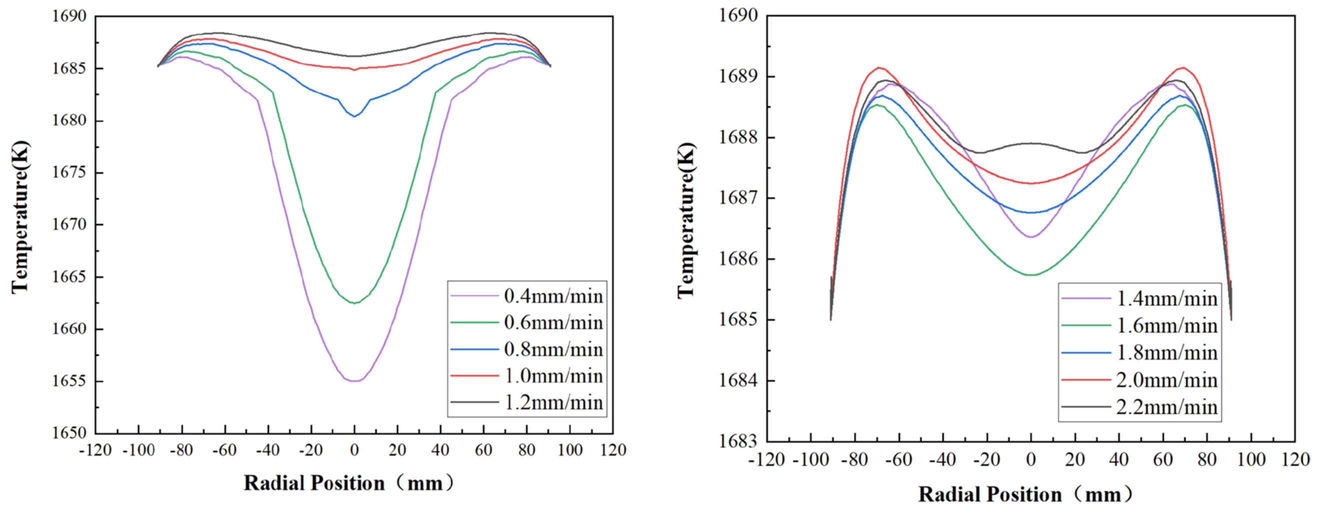

Fig. 6 Temperature distribution of triple point cross-section at different pulling speeds

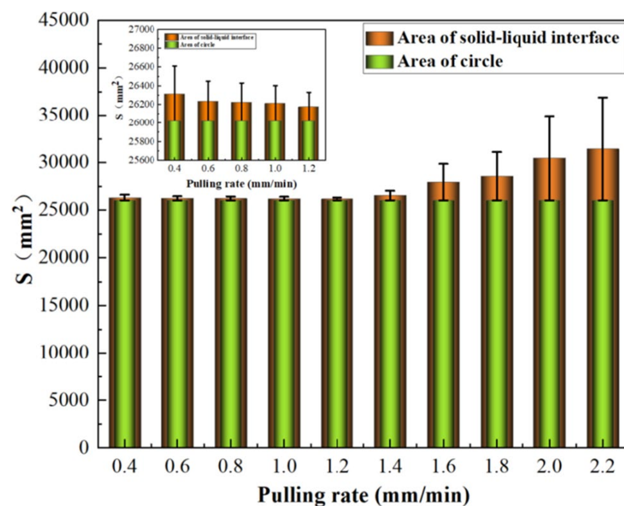

Fig. 7 Variation of S-L interface area at different pulling speeds

silicon rod is the center of the circle, and the radius of the single-crystal silicon rod is R. When the solid–liquid interface is n-shaped, the temperature at R on the three-phase point cross section is the lowest, and the temperature at about $\frac{2}{3}$R is the highest. A thorough comparison of Figs. 4 and 6 reveals that the alteration of pulling speed triggers modifications both in the rate at which heat is dissipated per unit time in single crystal silicon rods (i.e. the thermal field), and in the rate and direction of molten material flow (i.e. the flow field). Hence, alterations in the shape of the S-L interface stem from the dual influence of the heat and flow fields during the production of single-crystal silicon.

As well, the S-L interface area was extracted from the 3D shape, and the area changed at different casting speeds as shown in Fig. 7. As the shape of the S-L interface changes from m-shaped to ⌒-shaped, the area of the S-L interface decreases slowly until it reaches the cross-sectional area of a single-crystal silicon rod of equal diameter; as the shape of the S-L interface changes from ⌒-shaped to n-shaped, the area of the S-L interface gradually decreases increase, and the amplitude of change is much greater than when it changes from m-shaped to ⌒-shaped. There may be a certain reference value in this result for the study of impurity diffusion during the growth of single-crystal silicon.

3.2 Effect of Solid–Liquid Interface Shape on Stress

Dislocations are generally the result of thermal shear stress generated during the crystallization process, and these thermal shear stresses exceed the critical shear stress, causing plastic deformation of the crystal. A crystal exhibits anisotropy, with differing densities of the atomic arrangement and interatomic spacing in different directions leading to variations in both the amount of heat absorbed and the rate of heat transfer, thus resulting in distinct thermal conductivity coefficients and thermal expansion coefficients in various directions of the crystal. Single-crystal silicon belongs to a class of materials that possess the inherent characteristics of a crystal. The von Mises criterion, introduced by Hans von Mises in 1913, is a yield criterion. The von Mises criterion is frequently employed in elastoplastic mechanics as a criterion for evaluating material fatigue and failure. The von Mises yield criterion is stated as follows: Under certain deformation conditions, when the equivalent stress at a point within a loaded body reaches a certain value, that point begins to enter a plastic state. The von Mises stress criterion is utilized to represent the level of thermal stress and provides an estimation of the level of total shear stress in a crystal. A crystal region with a high probability of dislocation generation can

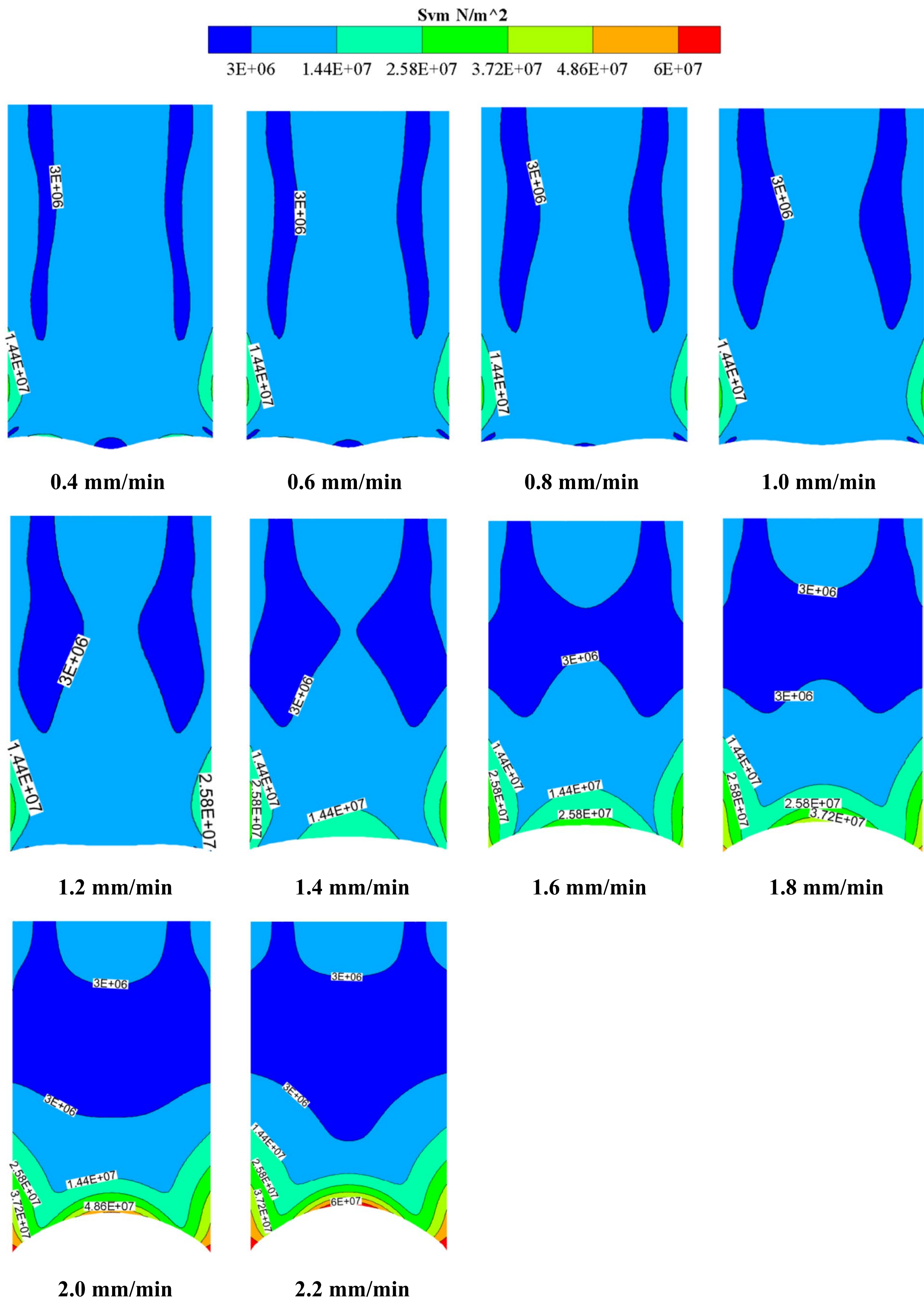

Fig. 8 S_{VM} distribution of ingots near the S-L interface under different pulling speeds

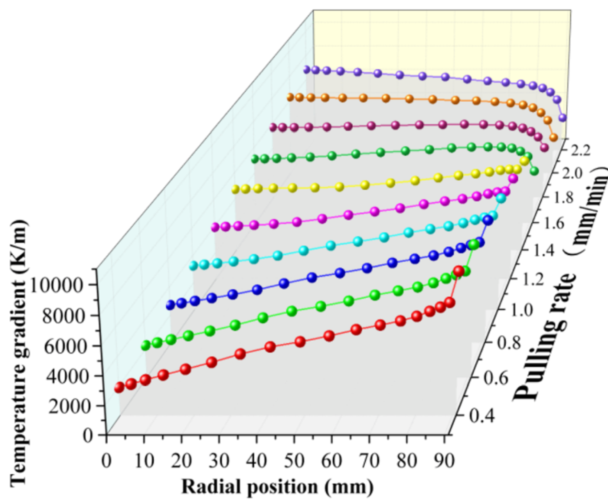

(a) Temperature gradient

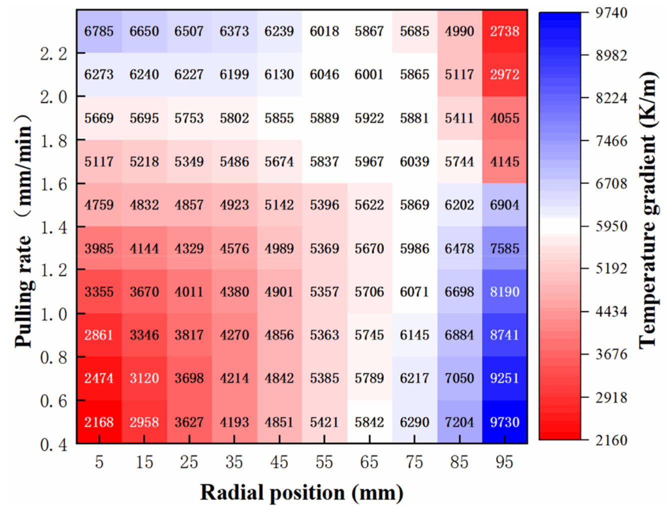

(b) Axial temperature difference

Fig. 9 Temperature gradient at each point on the solidification interface

be evaluated by evaluating the ratio of the von Mises stress to the critical shear stress, which is referred to as an excess stress field.

3.2.1 Effect of Solid–Liquid Interface Shape on von Mises Stress

In 1980, Jordan et al. first applied the critical resolved shear stress (CRSS) model to the growth of single crystal materials using the CZ method [38–43]. The following criteria are used to judge polycrystalline materials:

$$\sigma_{VM} \leq \alpha\sigma_{CRSS} \tag{29}$$

where σ_{VM} is the von Mises stress, α is material dependent, and σ_{CRSS} is the critical shear stress. The critical shear stress takes into account the atomic interaction in the crystal, so it is related to the material and heat. A common expression of this parameter is:

$$\sigma_{CRSS} = 0.1 \times 10^{\left(\frac{a}{T}-b\right)} \tag{30}$$

where T is the absolute temperature, the constants a and b are related to the material, $a = 4406.08$、$b = -4.58$ for silicon。Particularly, when silicon is close to its melting point, $\sigma_{CRSS} = 1.85\text{MPa}$.

Von Mises stress is expressed as follows:

$$\sigma_{VM} = \sqrt{\frac{1}{2}\left[\left(\sigma_I - \sigma_{II}\right)^2 + \left(\sigma_{II} - \sigma_{III}\right)^2 + \left(\sigma_I - \sigma_{III}\right)^2\right]} \tag{31}$$

where σ_I、σ_{II} and σ_{III} stand for the first, second, and third principal stresses, respectively.

As shown in Fig. 8, the Von Mises stress distribution on the ingot near the S-L interface is affected at different speeds of crystal pulling. When the S-L interface is m-shaped, the minimum von Mises stress at the S-L interface appears at the center of the single-crystal silicon rod and the three-phase point. When the S-L interface is n-shaped, the von Mises stress value on the S-L interface is larger, and the maximum value appears at the three-phase point. When the S-L interface approaches ⌒-shape, the von Mises stress distribution on the S-L interface is the most uniform.

As shown in Fig. 9, the temperature gradient changes at the S-L interface at different crystal pulling rates. When the S-L interface is m-shaped, the temperature gradient at the

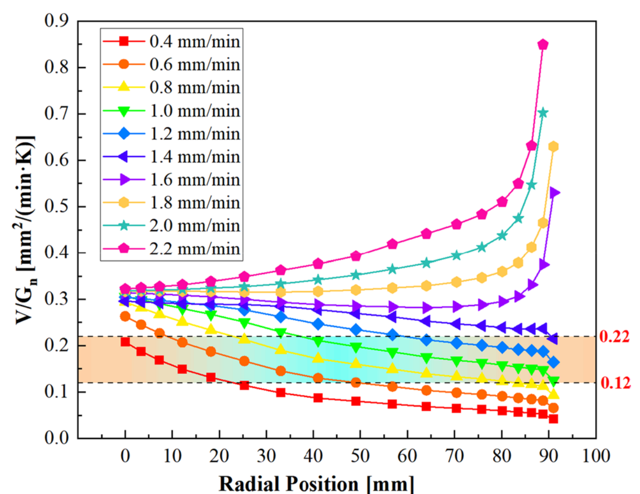

Fig. 10 The V / G value of S-L interface at different pulling rates

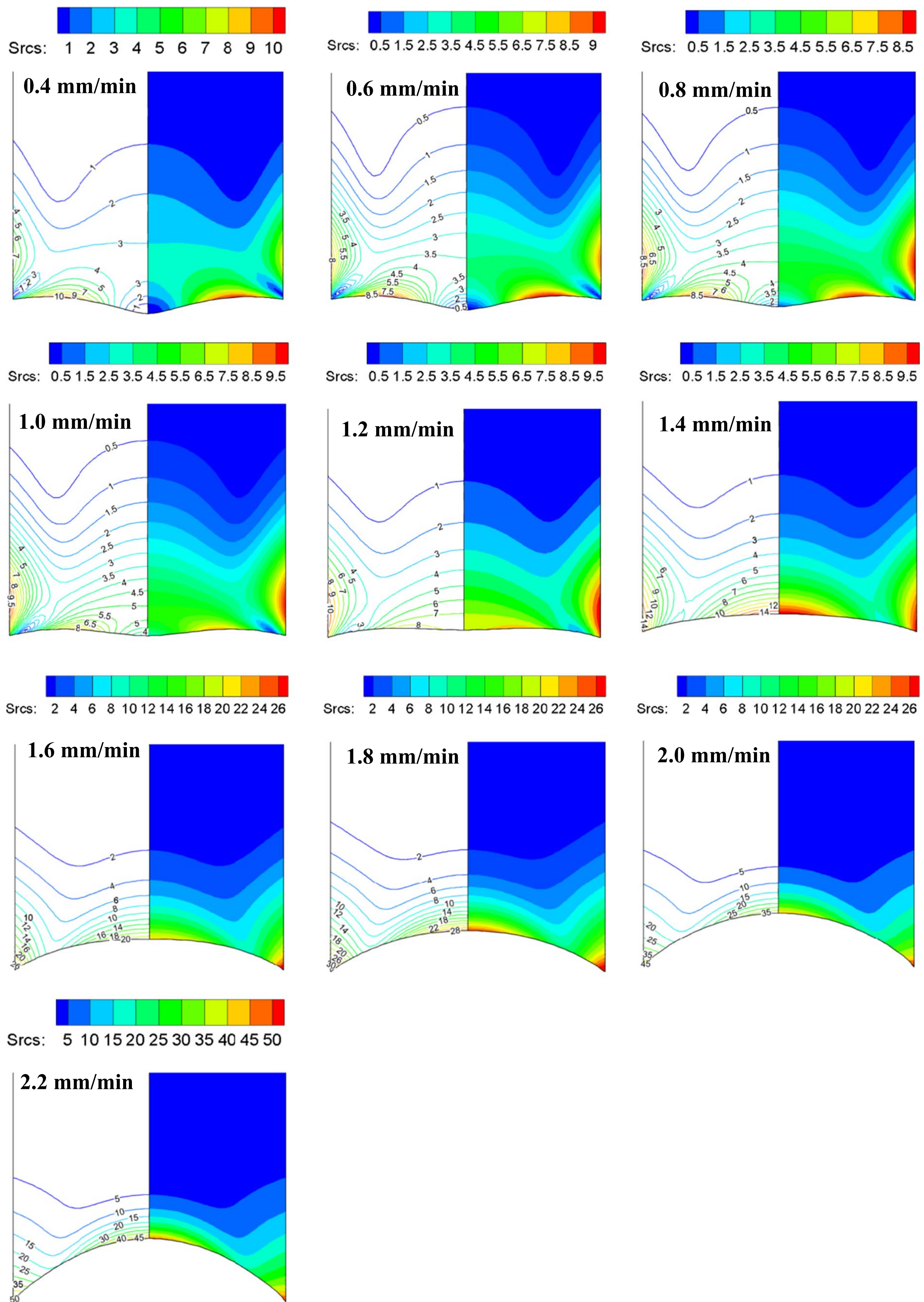

Fig. 11 S_{rcs} distribution near the S-L interface under different pulling speeds

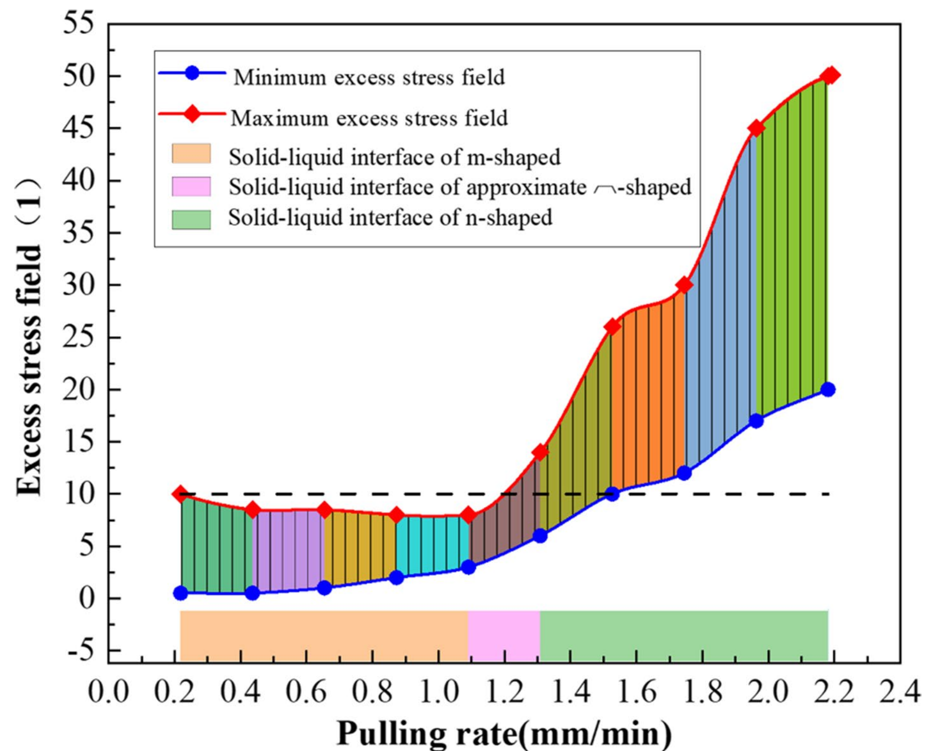

Fig. 12 Bandwidth diagram of excess stress field on S-L interface under different crystal pulling speeds

centre of the single-crystal bar is small and the temperature gradient at the edges is large. The opposite is true when the S-L interface is n-shaped. The larger temperature gradient in the axial direction facilitates the increase in the axial growth rate of single-crystal silicon.

According to the V/G theory, the center defect type of the single-crystal silicon rod grown at the m-shaped S-L interface is I-dominant, and the edge defect type is V-dominant; when the S-L interface is n-shaped, the opposite is true. The range of ξ_{cri} values in the literature varies slightly and is basically in the range of 0.12—0.22 mm^2/(min·K) [44, 9, 45, 46]. As shown in Fig. 10, when the shape of the S-L interface changes from m-shaped to n-shaped, most of the V/G values at the S-L interface are within ξ_{cri}. When the depth of the n-shaped S-L interface exceeds 10 mm, the V/G values at the S-L interface near the surface of the single-crystal silicon rod increase sharply. When the S-L interface is n-shaped, the V/G values at the S-L interface are all greater than 0.2 mm^2/(min·K), which means that single-crystal silicon point defects are dominated by V-dominant, which is favorable for the growth of PV single-crystal silicon [17]. Ideally, when the S-L interface is infinitely close to the ⌒-shaped, the radial temperature gradient of the single-crystalline silicon is most uniform and the defects in the grown single-crystal silicon rods are minimal. However, the structure of the thermal field dictates that the S-L interface cannot be ⌒-shape and, in terms of V/G, an n-shaped S-L interface with a depth of 10–20 mm is most favorable for the growth of single-crystal silicon.

3.2.2 Evaluation of Dislocation by Solid–Liquid Interface Shape

As a qualitative criterion for preventing single crystals from entering plasticity, the ratio of the von Mises stress to the critical partial shear stress (excess stress field) was used. The excessive stress field range of 1 ~ 10 should be satisfied for no dislocation in single-crystal silicon.

$$\frac{\sigma_{VM}}{\sigma_{CRSS}} \leq 1 \sim 10 \tag{32}$$

As shown in Fig. 11, the distribution of excess stress field near the S-L interface at different crystal pulling speeds is shown. When the S-L interface is m-shaped, the excess stress field on the S-L interface decreases as pulling speed increases and the excess stress field near the S-L interface is less than 10; when the S-L interface approaches ⌒-shape, the upper excess stress field on the S-L interface is the smallest; when the S-L interface is n-shaped, the excess stress field on the S-L interface increases with pulling speed, and the maximum excess stress field exceeds 10.

As shown in Fig. 12, the bandwidth of the stress field on the S-L interface at different crystal pulling rates is depicted. Whenever the S-L interface is m-shaped, the excess stress field distribution bandwidth decreases, and the excess stress field distribution on the S-L interface is uniform; when the S-L interface approaches ⌒-shape, the excess stress field distribution bandwidth is the lowest rate for all three S-L

interface shapes, and the excess stress field distribution on the S-L interface is also most uniform; when the S-L interface is n-shaped, with an increase in pulling speed, the excess stress field distribution bandwidth increases.

4 Conclusion

In this study, we numerically simulated the relationship between the S-L interface shape and the thermal stress during the continuous change of the pulling speed. The results of the study show that:

(1) At the equal-diameter growth stage, as the crystal pulling speed increases, the shape of the S-L interface changes from the m-shape to the ⌒-shape and then to the n-shape, while the area of the S-L interface decreases and then increases.
(2) The von Mises stress on the S-L interface is homogenized as the S-L interface approaches the cross-sectional area of the single-crystal silicon rod at the equal diameter stage. The triple point of Von Mises stress concentration appears with increasing crystal pulling speed.
(3) When the S-L interface changes from m-shape to ⌒-shape, the excess stress field decreases and its value is less than 10. When the shape of the SL interface changes from ⌒-shape to n-shape, the excess stress field increases, and its value is greater than 10.
(4) It is observed that excessive stress is large during the growth process of Cz-Si when pulling speed is high, and small when pulling speed is low. The fluctuating pulling speed assists in the release of stress during the crystal growth process and enhances the quality of the crystal. Single-crystal silicon is most conducive to growth at a S-L interface with a depth of 10–20 mm when the V/G value is slightly greater than 0.22.

Acknowledgements The authors are grateful for the financial support by Key Research and Development Project of Yunnan Province (No.202002AB080030 and No.202103AA080003), Major Science and Technology Projects in Yunnan Province (No.202102AB080016 and No.202202AG050012).

Author Contributions All authors contributed to the study conception and design. Model building, data collection and analysis were performed by Tai Li, Liang Zhao and Zhenling Huang. The first draft of the manuscript was written by Tai Li and all authors commented on previous versions of the manuscript. All authors read and approved the final manuscript.

Funding None.

Data Availability The datasets generated during and/or analysed during the current study are available from the corresponding author on reasonable request.

Declarations

Ethics Approval Not applicable.

Consent to Participate All the authors have complete consent to participate.

Consent for Publication All the authors have complete consent for publication.

Competing Interests The authors declare no competing interests.

References

1. I. E. A. (IEA) World Energy Outlook 2020. https://www.iea.org/reports/world-energy-outlook-2020. Accessed 18 Jan 2023
2. Saga T (2010) Advances in crystalline silicon solar cell technology for industrial mass production. NPG Asia Mater 2(3):96–102
3. Lan CW, Hsieh CK, Hsu WC (2009) Czochralski silicon crystal growth for photovoltaic applications. In Crystal growth of Si for solar cells. Springer Berlin Heidelberg, pp 25–39. https://doi.org/10.1007/978-3-642-02044-5_2
4. See. International Technology Roadmap for Photovoltaic (ITRPV). https://www.vdma.org/international-technology-roadmap-photovoltaic. Accessed 18 Jan 2023
5. Dash WC (1959) Growth of silicon crystals free from dislocations. J Appl Phys 30(4):459–474
6. Wang Z, Zhu X, Yuan S, Yu X, Yang D (2022) Comprehensive characterization of efficiency limiting defects in the swirl-shaped region of Czochralski silicon. Solar Energy Mater Sol Cells 236:111533 (2022/03/01/)
7. Suewaka R, Nishizawa SI (2023) Impact of Marangoni effect of oxygen on solid–liquid interface shape during Czochralski Silicon growth applied with transverse magnetic field. J Cryst Growth 607:127123. https://doi.org/10.1016/j.jcrysgro.2023.127123
8. Voronkov V (1982) The mechanism of swirl defects formation in silicon. J Cryst Growth 59(3):625–643
9. Voronkov VV, Falster R (1999) Vacancy and self-interstitial concentration incorporated into growing silicon crystals. J Appl Phys 86(11):5975–5982
10. Nakamura K, Maeda S, Togawa S, Saishoji T, Tomioka J (2000) Effect of the shape of crystal-melt interface on point defect reaction in silicon crystals. Proceedings of SPIE - The International Society for Optical Engineering 4218:31–43
11. Kalaev V, Lukanin D, Zabelin V, Makarov YN, Virbulis J, Dornberger E, Von Ammon W (2003) Calculation of bulk defects in CZ Si growth: impact of melt turbulent fluctuations. J Cryst Growth 250(1–2):203–208
12. Nakamura K, Suewaka R, Ko B (2014) Experimental study of the impact of stress on the point defect incorporation during silicon growth. ECS Solid State Lett 3(3):N5
13. Suewaka R, Nakamura K (2019) Effect of thermal stress on point defect behavior during single crystal Si growth. Jpn J Appl Phys 59(1):015502
14. Huang L, Lee P, Hsieh C, Hsu W, Lan C (2004) On the hot-zone design of Czochralski silicon growth for photovoltaic applications. J Cryst Growth 261(4):433–443

15. Sim B-C, Jung Y-H, Lee J-E, Lee H-W (2007) Effect of the crystal–melt interface on the grown-in defects in silicon CZ growth. J Cryst Growth 299(1):152–157
16. Smirnova O, Durnev N, Shandrakova K, Mizitov E, Soklakov V (2008) Optimization of furnace design and growth parameters for Si Cz growth, using numerical simulation. J Cryst Growth 310(7–9):2185–2191
17. Su W, Zuo R, Mazaev K, Kalaev V (2010) Optimization of crystal growth by changes of flow guide, radiation shield and sidewall insulation in Cz Si furnace. J Cryst Growth 312(4):495–501
18. Prostomolotov A, Verezub N, Mezhennii M, Reznik VY (2011) Thermal optimization of CZ bulk growth and wafer annealing for crystalline dislocation-free silicon. J Cryst Growth 318(1):187–192
19. Vizman D, Dadzis K, Friedrich J (2013) Numerical parameter studies of 3D melt flow and interface shape for directional solidification of silicon in a traveling magnetic field. J Cryst Growth 381:169–178
20. Daggolu P, Ryu JW, Galyukov A, Kondratyev A (2016) Analysis of the effect of symmetric/asymmetric CUSP magnetic fields on melt/crystal interface during Czochralski silicon growth. J Cryst Growth 452:22–26
21. Liu X, Nakano S, Kakimoto K (2017) Effect of the packing structure of silicon chunks on the melting process and carbon reduction in Czochralski silicon crystal growth. J Cryst Growth 468:595–600
22. Zhao W, Liu L (2017) Control of heat transfer in continuous-feeding Czochralski-silicon crystal growth with a water-cooled jacket. J Cryst Growth 458:31–36
23. Shiraishi Y, Maeda S, Nakamura K (2004) Prediction of solid–liquid interface shape during CZ Si crystal growth using experimental and global simulation. J Cryst Growth 266(1):28–33 (2004/05/15/)
24. Kalaev V, Evstratov IY, Makarov YN (2003) Gas flow effect on global heat transport and melt convection in Czochralski silicon growth. J Cryst Growth 249(1–2):87–99
25. Son S-S, Yi K-W (2005) Experimental study on the effect of crystal and crucible rotations on the thermal and velocity field in a low Prandtl number melt in a large crucible. J Cryst Growth 275(1–2):e249–e257
26. Nam P-O, Sang-Kun O, Yi K-W (2008) 3-D time-dependent numerical model of flow patterns within a large-scale Czochralski system. J Cryst Growth 310(7–9):2126–2133
27. Fujiwara K, Gotoh R, Yang X, Koizumi H, Nozawa J, Uda S (2011) Morphological transformation of a crystal–melt interface during unidirectional growth of silicon. Acta Mater 59(11):4700–4708
28. Noghabi OA, M'Hamdi M, Jomâa M (2011) Effect of crystal and crucible rotations on the interface shape of Czochralski grown silicon single crystals. J Cryst Growth 318(1):173–177
29. Noghabi OA, Jomâa M, M'hamdi M (2013) Analysis of W-shape melt/crystal interface formation in Czochralski silicon crystal growth. J Cryst Growth 362:77–82
30. Teng R, Chang Q, Li Y, Cui B, Xiao Q-H, Zhang G-H (2017) Numerical analysis of solid–liquid interface shape during large-size single crystalline silicon with Czochralski method. Rare Met 36(4):289–294
31. Liu L, Nakano S, Kakimoto K (2005) An analysis of temperature distribution near the melt–crystal interface in silicon Czochralski growth with a transverse magnetic field. J Cryst Growth 282(1–2):49–59
32. Assaker R (1998) Magnetohydrodynamics in crystal growth. PhD thesis, Université catholique de Louvain
33. Winckelmans G, Dupret F (1998) Private communication
34. Dupret F (2013) wxFEMAG 2.0 *[Computer software]*. FEMAG Company
35. Gao B, Kakimoto K (2010) Global simulation of coupled carbon and oxygen transport in a Czochralski furnace for silicon crystal growth. J Cryst Growth 312(20):2972–2976
36. Teng Y-Y, Chen J-C, Lu C-W, Chen C-Y (2010) The carbon distribution in multicrystalline silicon ingots grown using the directional solidification process. J Cryst Growth 312(8):1282–1290
37. Li T, Zhao L, Lv G, Ma W, Zhang M, Huang Z, Zhao L (2023) Thermodynamic analysis of dissolved oxygen in a silicon melt and the effect of processing parameters on the oxygen distribution in single-crystal silicon during Czochralski growth. Silicon 15(2):1049–1062
38. Duseaux M (1983) Temperature profile and thermal stress calculations in GaAs crystals growing from the melt. J Cryst Growth 61(3):576–590. https://doi.org/10.1016/0022-0248(83)90186-0
39. Jordan AS, Caruso R, Von Neida A (1980) A thermoelastic analysis of dislocation generation in pulled GaAs crystals. Bell Syst Tech J 59(4):593–637
40. Meduoye GO, Bacon DJ, Evans KE (1991) Computer modelling of temperature and stress distributions in LEC-grown GaAs crystals. J Cryst Growth 108(3–4):627–636. https://doi.org/10.1016/0022-0248(91)90242-W
41. Motakef S, Witt AF (1987) Thermoelastic analysis of GaAs in LEC growth configuration. J Cryst Growth 96(1):201–216. https://doi.org/10.1016/0022-0248(87)90521-5
42. Mullin JB (2004) Progress in the melt growth of III–V compounds. J Cryst Growth 264(4):578–592. https://doi.org/10.1016/j.jcrysgro.2003.12.036
43. Parfeniuk C, Weinberg F, Samarasekera IV, Schvezov C, Li L (1992) Measured critical resolved shear stress and calculated temperature and stress fields during growth of CdZnTe. J Cryst Growth 119(3–4):261–270. https://doi.org/10.1016/0022-0248(92)90678-C
44. Voronkov VV (1982) The mechanism of swirl defects formation in silicon. J Cryst Growth 59(3):625–643. https://doi.org/10.1016/0022-0248(82)90386-4
45. Voronkov VV (2000) Formation of voids and oxide particles in silicon crystals. Mater Sci Eng B-Solid State Mater Adv Technol 73(1–3):69–76
46. Voronkov VV, Falster R (2002) Intrinsic point defects and impurities in silicon crystal growth. J Electrochem Soc 149(3):G167. https://doi.org/10.1149/1.1435361

Publisher's Note Springer Nature remains neutral with regard to jurisdictional claims in published maps and institutional affiliations.

Springer Nature or its licensor (e.g. a society or other partner) holds exclusive rights to this article under a publishing agreement with the author(s) or other rightsholder(s); author self-archiving of the accepted manuscript version of this article is solely governed by the terms of such publishing agreement and applicable law.